Paper 137

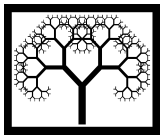

Proceedings of the Eleventh International Conference
on Computational Structures Technology,
B.H.V. Topping, (Editor),
Civil-Comp Press, Stirlingshire, Scotland

Assessment of the Dynamic Characteristics of a Ballasted Railway Track subject to Impact Excitation using Three-Dimensional Composite Finite Element - Discrete Element Modelling

A. Aikawa
Railway Technical Research Institute, Kokubunji, Tokyo, Japan

Abstract

Ballast grains transmit an impact load to the roadbed through multi-contact loading conditions in the boundary layers separating individual ballasts. In a ballasted track, the impact load within the aggregate of ballast grains affects the transmission characteristics, which in turn affect the plastic deformation that progresses as a result of the movement and wear of ballast grains. This paper describes a finite element vibration analysis of a ballast aggregate to examine frequency characteristics up to high-frequencies. The modelling method used ballast stones expressed as a polyhedron model using a three-dimensional discrete element method. A finite element model was built based on the numerical arrangement and contact data of the ballast stones. Inputting a train load and a hammer impulse to this model simulates its behaviour and clarifies the stress distribution of the ballast aggregate with respect to the impulse loadings, while also clarifying characteristics of the vibration and the wave propagation of the ballast stone aggregate by vibration analysis conducted using this model.

Keywords: distinct element method, finite element method, ballasted track, vibration analysis, wave propagation.

1 Introduction

Railway ballast generally consists of an assemblage of irregularly shaped, large, angular, and hard ballast particles, which transmit an impact load to the roadbed through multi-contact loading conditions that exist in the boundary layers separating individual ballasts. During a train's passage at high speed, each ballast particle receives a dynamic load at low frequency (up to several tens of Hertz) because of axle load passage. Each ballast particle also receives an impact load at high frequency (from a few hundred Hertz up to a million Hertz) excited by the rolling contact mechanism between a wheel and rail through a sleeper bottom. The frequent

passage of trains on tracks loosens and deforms the ballast and the supporting bed. Therefore, the ballast requires periodic maintenance work that entails high maintenance costs.

In the ballasted track, the transmission characteristics of the impact load in the aggregate of ballast grains affect the plastic deformation that progresses because of the movement and wear of ballast grains. The ballast particles' sharp corners lead to stress concentration and complex multi-contact stress distribution of a narrow area of blocks, which contributes to shearing resistance. Although particle abrasion, breakage, and movement are the main causes of ballast degradation, Lu and McDowell [1] explained that most ballast degradation is attributable primarily to corner breakage. However, load propagation characteristics inside ballast particles and between particles, in addition to elastic deformation characteristics inside and among particles, remain unexplained.

Figure 1 presents an outline of a ballasted track deterioration model. To clarify the transmission characteristics of a dynamic load within the ballast layer, this paper describes newly developed techniques for use in three-dimensional dynamic numerical model studies of a ballasted railway track. Results obtained using the technique are used to evaluate the dynamic behaviour of ballast aggregate and to elucidate impact-load-induced wave propagation inside ballast grains.

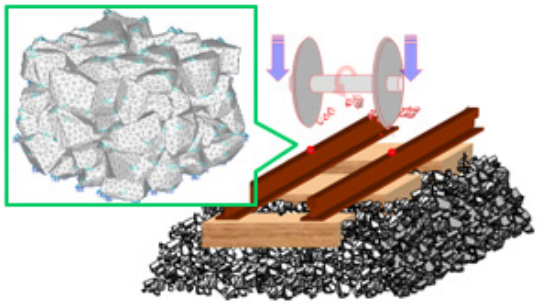

Figure 1: Outline of ballasted track deterioration model.

2 Modelling of ballast particles and finite element normal mode analysis

2.1 Particle shape digitalization

The author first measured the coordinates of vertices of about 4,000 ballast particles using a contact-type three-dimensional digitizer (MicroScribe-G2, measurement accuracy 35 mm; Immersion Corp.). Figure 2 portrays the measurement instruments. If the switch pedal attached to the equipment is depressed, then the three-dimensional coordinates at the tip of the digitizer probe are measured automatically and sent to the PC as text data [2].

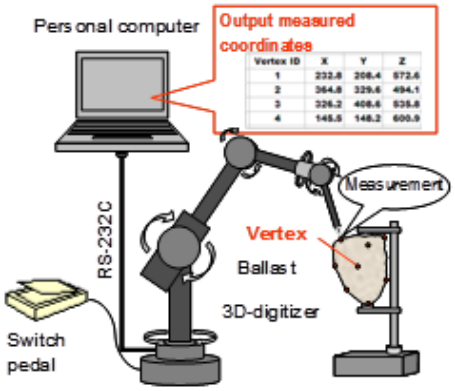

Figure 2: Digitization of particle shape.

2.2 Automatic generation algorithm for a numerical-value-shaped polyhedron

Based on the measured vertices–coordinates, with mutual connection of the vertices in straight lines, the configuration of each crushed stone can be represented numerically as a three-dimensional polyhedron consisting of an assemblage of triangular planes. The automatic generation algorithm was newly developed to determine the polyhedron shapes objectively and efficiently from the measured vertices–coordinates. The algorithm is based on two viewpoints: (1) a polyhedron consists of a set of triangles, and (2) a polyhedron becomes convexly configured to the greatest degree possible. Figure 3 presents exemplary pictures of existing ballasts and the digitized models based on the numerical data by measurement. According to the algorithm, the measured vertices–coordinates are expressed numerically as DE polyhedron models.

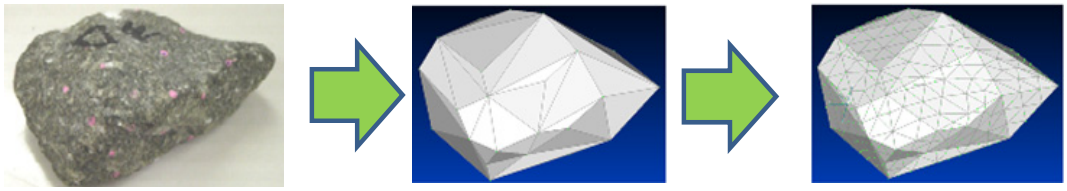

(a) Ballast (b) DEM Model (c) FEM Model

Figure 3: Exemplary pictures of existing ballasts and the digitized models.

2.3 Finite element modelling for individual ballast particles

The individual DE polyhedral models are converted into aggregates of the solid tetrahedral finite element meshes (3D second-order finite element elements) having intermediate nodes between the edge pairs. We adopted 10 mm mesh size, which is sufficiently fine to produce reliable stress information, to represent the stress distribution correctly, to detect local stress concentrations, and to represent the

normal modes frequencies precisely. Figure 3 shows that the generated polyhedron models and finite element aggregates model can well reproduce the actual angularity geometries of ballast stones.

2.4 Physical properties of ballasts

Table 1 presents physical properties of ballast such as density, Young's modulus, and Poisson's ratio used for this study. The density of ballast particles was the laboratory experimental value obtained from specific gravity tests. Young's moduli and Poisson's ratio were derived from previous reports in the literature. Regarding the structural damping coefficient, we adopted the general values of a concrete structure.

Item	Ballast
Density ρ	2700 (kg/m^3)
Young's Modulus E	30 (GPa)
Poisson's ratio ν	0.2
Structural damping parameters η	0.01

Table 1. Physical properties of ballasts.

2.4 Normal mode analysis for individual ballast particles

After converting individual DE polyhedron models to aggregates of the finite element tetrahedral models, the author performed 60 cases of finite element normal mode analysis, which yielded a set of normal modes for individual ballast particles. Figure 4 shows an exemplary result of normal mode analysis related to first-order, second-order, and third-order normal modes of a ballast particle. The contours in each figure show von Mises strain values. As the figure shows, the first, second, and third normal modes are the respective modes accompanied by elastic deformation such as bending and torsion for the ballast particle body.

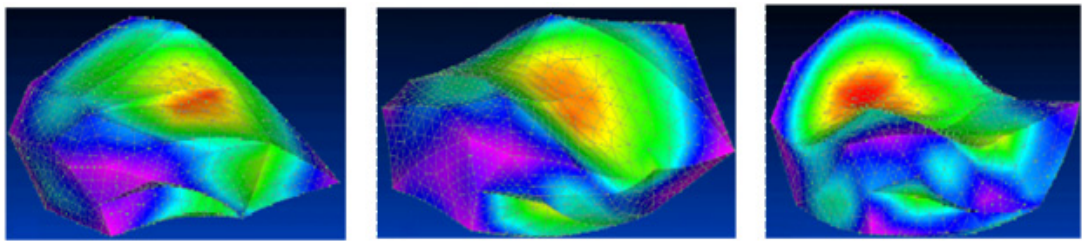

(a) First-Order (13.3 kHz) (b) Second-Order (15.0 kHz) (c) Third-Order (20.2 kHz)

Figure 4: Exemplary result of normal mode analysis.

Figure 5 portrays the relation between the first-order natural frequency and second-order natural frequency with respect to 60 ballast particles. All natural frequencies of

ballast particles were identified in the very high-frequency domain of more than 11 kHz. In addition, Figure 6 shows the average values and standard deviations of natural frequencies related to normal modes from first-order to fourth-order.

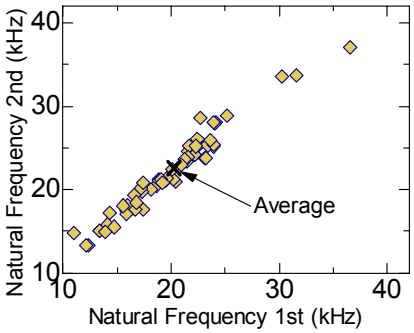

Figure 5: Distribution of natural frequencies.

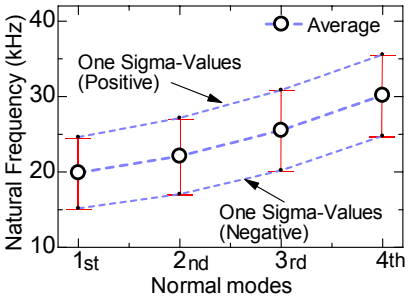

Figure 6: Average values of natural frequencies.

3 Modelling of ballast aggregate and its finite element normal mode analysis

3.1 Compaction procedure using 3D-DEM

Figure 7 shows the procedure for creation of a finite element model of the ballast aggregate. First, 89 pieces of the individual ballast model (polyhedral rigid body DE model) were placed randomly and homogeneously in the air above the rectangular box frames placed on the roadbed. Then, the blocks were allowed to fall freely and were compressed with a loading plate from the ballast upper surface by application of a discrete element method: *3DEC* [3]. The time-dependent 10 kN homogeneous loading was added to the loading plates. After 0.5 s of compaction, the plates were separated from the ballast and the blocks were left unloaded for 1.0 s. In this case, the value of normal stiffness between ballast particles was set to an extremely large value (2000 GPa/m) to reduce the amount of penetration between ballast particles. Moreover, the friction angle between ballast particles was set to a small value (5 deg) so that the ballast particles might be compacted efficiently.

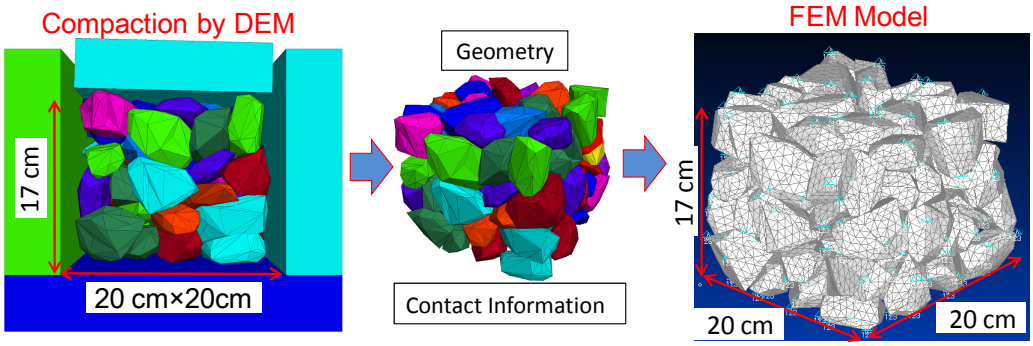

Figure 7: Procedure for creation of a finite element model of the ballast aggregate.

3.2 Finite element modelling of ballast aggregate

Next, the author converted all individual ballast particles (polyhedron DE rigid models) into clumps consisting of small finite element elements (tetrahedron second-order elastic elements) split within 10 mm mesh sizes, while maintaining their geometry and contact-point information. Each polyhedron DE rigid model was divided into 4000–5000 pieces of tetrahedron finite element elastic elements. The dimensions of the finished finite element analysis model were 20 cm width, 20 cm length, and 17 cm height. The whole model comprises more than 460 thousand tetrahedron finite elements.

The contact-point information between ballast particles was modelled as a set of extremely hard 3D springs (spring stiffness k = 300 GN/m) with no length, which connect the nodes of elements with each other in three axial directions related to the contact pair of blocks at each contact point. The contact spring stiffness was set to such an extremely stiffer value than stiffness of the tetrahedron finite elements that the contact springs would be almost unchanged in shape against any external force. This analysis ignored frictional effects, using only mutually connected contact pairs. Therefore, the spring functions acting on the contact points were represented by the local deformation of angularities of ballasts composed by the assemblage of several tetrahedron finite elements adjacent to the contact points.

3.3 Finite element normal mode analysis of ballast aggregate

By applying finite element normal mode analysis for the ballast aggregate finite element model, the author obtained the set of normal modes related to the ballast aggregate. Figure 8 shows the first-order natural frequency mode of the ballast aggregate obtained from the numerical result of normal mode analysis. As the figure shows, the first-order natural frequency mode of the ballast aggregate is such that the whole ballast aggregate would repeat vertically elastic expansion–shrinkage motions while obviating the restrictions of the square frame.

The normal frequency of the first-order normal mode, which represents the vertical motion of the entire aggregate, is 1715 Hz, which is much lower than the

normal frequency of the individual particles. The respective normal frequencies of second-order and third-order normal modes are 1980 Hz and 2030 Hz. The actual ballast structure is larger than this model. Therefore, the results indicated that the actual ballast will have a similar normal mode in the lower frequency domain to that of the analytical result.

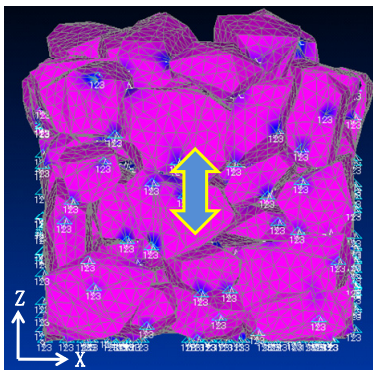

Figure 8: The first-order natural frequency mode (side view).

Figure 9 depicts the distribution of strain with respect to the horizontal cross-sectional plane of which the height is 0.132 m. As the figure shows, only several angularities (sharp edges) are adjacent to the contact points. Among all angularities of the ballast aggregate, only they would deform locally and act as elastic springs. Most other parts of the ballast aggregate would vibrate as a rigid body. The results show that the dynamic loads acting on a ballast aggregate are not supported uniformly all over the ballast particles within the ballast aggregate. They vary greatly in relation to location and concentrate on some contact points among all angularities. These results indicate that when the dynamic loads act on a ballast aggregate, most portions in the ballast aggregate homogeneously vibrate elastically. Nevertheless, only several specific angularities adjacent to the stress concentration areas vibrate violently.

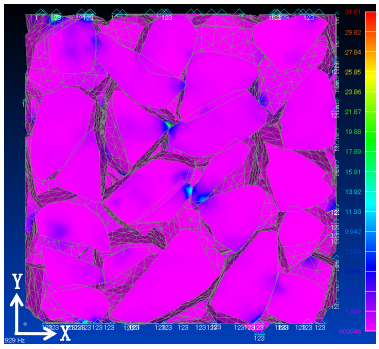

Figure 9: Stress distribution of the first-order natural frequency mode: top view of x-y cross-section (z = 0.132 m).

4 Responses of ballast aggregate to actual traffic loading

4.1 Measured loading waveforms

The time-history response waveforms of the internal stresses of ballast particles were calculated numerically by inputting the measured loading waveforms on the bottom surface of a sleeper when a passenger express train passed the top surface of the previously described ballast aggregate model.

Figure 10 shows actual waveforms of vertical loadings measured in an 8 cm × 8 cm cross-sectional area on the bottom surface of the sleeper imparted by first and second axles of a lead coach bogie when a passenger express train passed at 120 km/h through the test section [4]. As the figure shows, the first and second axles of a lead coach bogie passed immediately above the sleeper centre at around 0.06 s and 0.12 s, respectively. In the finite element analysis, the measured time history waveforms were uniformly inputted on the four points around a centre area of the top surface of the ballast aggregate model. The calculating time interval was set to $\Delta t = 1.0\times10^{-5}$ s.

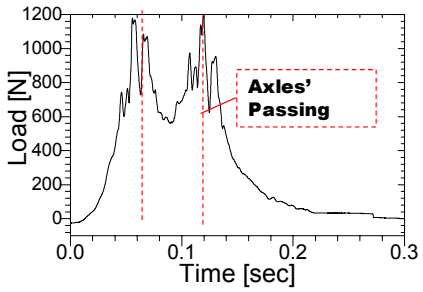

Figure 10: Measured waveform of loading on the bottom surface of sleeper.

4.2 Internal stress distribution of ballast aggregate

Figure 11 shows the von Mises stress distribution in the ballast aggregate at the time of $t = 0.055$ s, when the load peaks appeared, at which time the first axle of a lead coach bogie passed immediately above the sleeper centre. The figure indicates that the dynamic stress of ballast induced by a passing train was not distributed uniformly throughout the ballast aggregates. The large stresses are concentrated locally around the specific contact points. The analytical results show that the maximum stress within the time history, 43 MPa, occurred with external loading of 1.2 kN (0.1875 MPa).

Although the magnitude of the analytical model was extremely small, the stress ratio of internal maximum stress to external loading reaches approximately 230 at least. The unconfined compression strength of ballast rocks was 60–100 MPa and maximum stress in this analysis is less than that value. However, we can readily estimate that failures in the angularities will occur around the stress concentration points when excessive dynamic external force acts on the ballast surface.

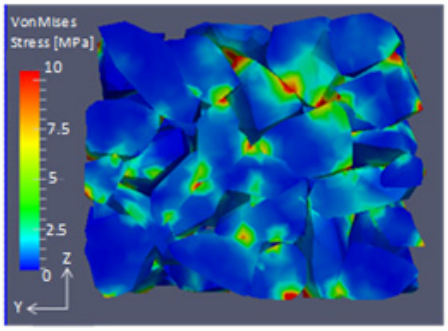

Figure 11: Internal stress distribution of ballast aggregate.

5 Wave propagation analysis in the ballast aggregate

The dynamic loadings added on the body surface propagate in the ballast aggregate as an impact wave. In this chapter, we performed the transient response analysis to evaluate wave propagation characteristics in the ballast aggregate against impact loadings.

5.1 Analytical conditions

Figure 12 presents the applied waveforms of vertical impact loadings and numerical models of two types: one is an intact rock model consisting of 6800 pieces of cubic elements 1 cm on each edge made with a continuous homogeneous elastic body. The model size is 20 cm × 20 cm × 17 cm. Another is a previously described model of the ballast aggregate. Time-dependent loading waveforms were applied vertically to the 8 cm × 8 cm areas around the centre of the top surface of each model, respectively. The loadings were a single rectangular pulse wave in the vertical direction only. By setting the amplitude and pulse length respectively to 10 kN and 5 μs, the author calculated the stress distribution characteristics of the ballast aggregate at every time step of $\Delta t = 1.0\times10^{-6}$ s.

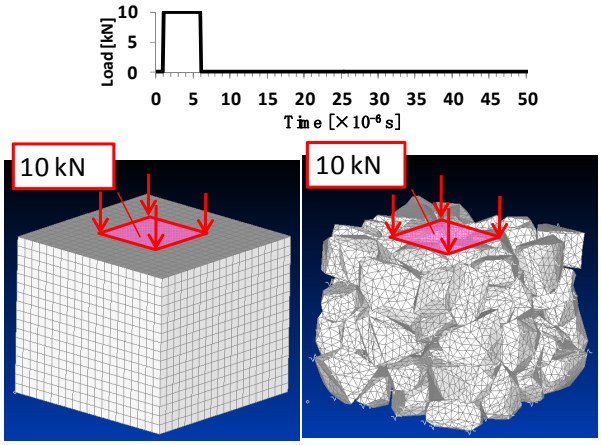

(a) Intact Rock (b) Ballast Aggregate

Figure 12: Models and Impact load.

5.2 Stress distributions

Figure 13 shows the distribution of von Mises stress on the vertical section passing through the central axis at each time step.

For the case of the intact rock from Figure 13(a), the impulse wave propagates, with gradual spreading, downward with uniform velocity. It reaches the bottom face at the time of 47 μs.

In contrast, for the case of the ballast aggregate shown in Figure 13(b), the impulse wave is transmitted in general through complicated courses by the following four steps: (1) The impulse wave and hammer hitting propagated through the inner part of the rock, which was hit by an impulse hammer at the same speed as in the case of the intact rock. (2) Almost all waves stay in the inner part of the rock and repeat diffusion and reflection. (3) Some waves, which reached at the contact points with other rocks, are transmitted to the rocks which adjoin through contact points. (4) The waves, which reached the adjoining rock, diffuse the inner part of the adjoining rock. Some of them propagate to the next rock further in contact points.

At 60 μs of time in Figure 13(b), the wave leading edge reaches the middle part of the model, but many strong waves repeatedly diffuse and reflect in the inner parts of the upper rocks.

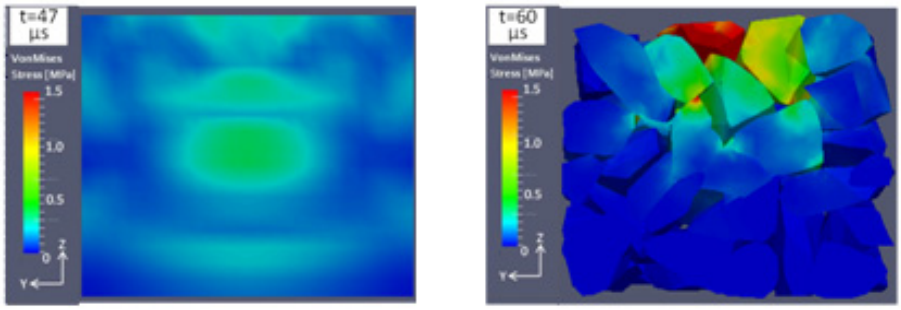

(a) Intact Rock (b) Ballast Aggregate

Figure 13: Distribution of von Mises stress on the vertical section.

5.3 Time history response of contact stress

Figure 14 presents the time history response waveforms of von Mises stresses for four arbitrary contact points located at different depths near the central line under the loading points. The figure indicates that, as measuring points become increasingly distant from the loading point, high-frequency vibrating components decrease, waves become smooth, and the times at which each peak response occurs in each time history of stress waveforms becomes later.

Based on the time of occurrence of the peak value in the time history of stress waveforms, the velocities of elastic waves were calculated for both models. The elastic wave velocity in intact rock reaches 3610 m/s whereas that in a ballast aggregate is only 710 m/s. In this analysis, results show that the velocity of the elastic wave in a ballast is reduced to one-fifth that of the velocity of the elastic

wave in intact rock. Generally the velocity of an elastic wave in a hard rock mass is 3000– 5000 m/s. That in a ballast aggregate is approximately 400 m/s. These analyses numerically reproduce the mechanisms by which the wave propagation velocity inside a ballast layer is reduced and by which a wave motion decreases greatly inside a ballast layer. Moreover, the analyses use only elastic body analysis, which does not incorporate material nonlinearity.

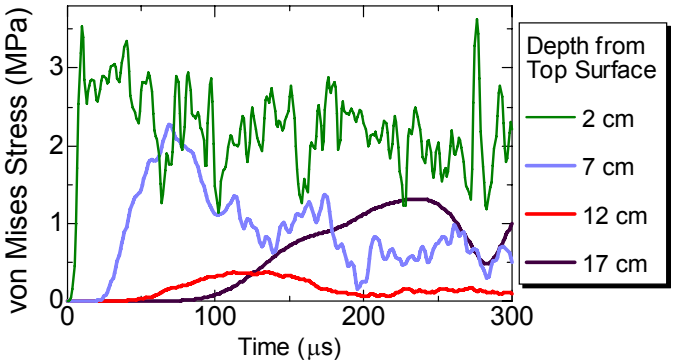

Figure 14: Time history response waveforms of von Mises stresses.

6 Conclusions

As described in this paper, modelling techniques were developed for use in 3D finite element studies of a ballasted railway track to clarify the transmission characteristics from low frequency up to high frequency against a dynamic load within the ballast layer. The results obtained using the technique were used to evaluate the dynamic behaviour of ballast aggregate and wave propagation inside the ballast grains when they are affected by impact loads. Explanations of analyses using an integrated approach combining finite element modelling and discrete element modelling are also given.

For individual ballast grains and the ballast aggregate structure, the author performed finite element normal mode analysis. All normal modes for individual ballast grains were identified in the very-high-frequency domain of more than 11 kHz. Application of finite element normal mode analysis for the ballast aggregate structure yielded a set of normal modes related to the ballast aggregate. The normal frequency of the first-order normal mode, which represents the vertical motion of the entire aggregate, is 1715 Hz, which is much lower than the normal frequency of the individual particles. An actual ballast structure is larger than this model, but the results indicated that the actual ballast in the lower frequency domain will have a similar normal mode to that of the analytical result.

Next, inputting measured train loads to the ballast aggregate model clarified that the dynamic stress of ballast induced by a passing train was not distributed uniformly throughout the ballast aggregates. Rather, large stresses concentrate locally around specific contact points. Moreover, the author, using only elastic body analysis which does not incorporate material nonlinearity, numerically reproduced

the mechanisms which reduce the wave propagation velocity inside a ballast layer and which greatly decrease a wave motion inside a ballast layer. These newly developed techniques are beneficial for analyzing 3D ballast motion induced by passing trains.

References

[1] M. Lu and G. R. McDowell, "Discrete Element Modelling of Railway Ballast under Triaxial Conditions", Geomechanics and Geoengineering, 3(4), 257-270, 2008.

[2] A. Aikawa, "DEM modeling techniques for dynamic analysis of ballasted railway track", *2nd International FLAC/DEM Symposium, Melbourne, Australia*, 2011.

[3] Itasca Consulting Group, Inc., "3DEC – 3 Dimensional Distinct Element Code, Ver. 4.10 User's Manual", Minneapolis, 2007.

[4] A. Aikawa, F. Urakawa, K. Abe, A. Namura, "Dynamic Characteristics of Railway Concrete Sleepers using Impact Excitation Techniques and Model Analysis", *WCRR*, 2011.